Pleural macrophages promote recovery from influenza virus infection

James P Stumpff II[1], Sang Yong Kim[2], Adriana Forero[3], Andrew Nishida[3], Yael Steuerman[4], Irit Gat-Viks[4], Meera G Nair[2], Juliet Morrison[1]

[1]Department of Microbiology and Plant Pathology, University of California, Riverside, CA, USA

[2]Division of Biomedical Sciences, School of Medicine, University of California, Riverside, CA, USA

[3]Department of Microbiology, University of Washington, Seattle, WA, USA

[4]Shmunis School of Biomedicine and Cancer Research, Faculty of Life Sciences, Tel Aviv University, Tel Aviv, 6997801, Israel

*Corresponding author

Juliet Morrison, PhD

Department of Microbiology and Plant Pathology

900 University Avenue

University of California

Riverside, CA 92521, USA

jmorriso@ucr.edu

ABSTRACT

Seasonal influenza results in 3 to 5 million cases of severe disease and 250,000 to 500,000 deaths annually. Macrophages have been implicated in both the resolution and the progression of the disease, but the drivers of these outcomes are poorly understood. We probed mouse lung transcriptomic datasets using the Digital Cell Quantifier algorithm to predict immune cell subsets that correlated with mild or severe influenza A virus (IAV) infection outcomes. This allowed us to identify a novel lung macrophage population that was transcriptionally similar to small serosal cavity macrophages and was only present in mice that survived IAV infection. Large serosal macrophages have been implicated as a source of macrophages for visceral organs in inflammatory diseases. However, until now, the study of serosal macrophage translocation in the context of infections, and the study of small serosal macrophage translocation in general has been neglected. We used flow cytometry and microscopy to show that fluorescently-labeled pleural macrophages (PMs) migrate from the pleural cavity into the lung after infection with A/California/04/2009 virus. The numbers of translocated PMs peak at day 9, which is during the resolution phase of the disease and after virus has been cleared. Our data show that PM recruitment to the lung parenchyma occurs across the mesothelial layer and not through the vasculature. Translocated PMs phenotypically resemble a MHCII^{hi} subpopulation of interstitial macrophages (IMs) that rapidly expands in number during influenza virus infection. Depletion of PMs prior to IAV infection led to increased morbidity when compared to the control group. Lack of PMs also resulted in increased pleural cavity inflammation and an influx of neutrophils within the lung. Our results show that both small and large PMs are recruited to the lung during IAV infection and contribute to recovery from influenza. This

study expands our knowledge of PM plasticity and provides a new source of IMs independent of monocyte recruitment and local proliferation.

INTRODUCTION

Influenza A virus (IAV) is responsible for seasonal epidemics and four pandemics that arose from a lack of immunity and human-to-human transmission [1]. Despite current vaccine strategies, IAV remains a major public health concern. Patient outcomes of influenza A virus (IAV) infections depend on the delicate balance between immune protection and immunopathology that is orchestrated by innate immune responses and subsequent adaptive immunity [2]. Further investigation into IAV outcomes is needed to understand the resolution of viral clearance and restoration of pulmonary homeostasis.

The host response to infection is an important determinant of influenza outcomes [3-7]. For example, severe influenza outcomes are associated with high levels of proinflammatory cytokines and leukocytes in the lung [5, 7, 8]. Patients hospitalized with severe seasonal IAV infections have a sustained increase in monocytes [9], and patients with severe avian influenza have elevated levels of inflammatory cytokines in their acute-phase sera [10-12]. Infection with highly pathogenic IAVs such as the 1918 virus and avian H5N1 virus leads to a massive recruitment of neutrophils and inflammatory macrophages to the lungs of mice [3, 4]. Depending on the virus strain, mice may develop progressive pneumonia characterized by extensive neutrophilia, hypercytokinemia, pulmonary edema, and reductions in alveolar gas exchange that are reminiscent of acute respiratory distress (ARDS) in human patients [13-16]. We previously identified lung transcriptomic signatures that distinguished mild and severe influenza outcomes in BALB/c mice infected with different IAV strains [17]. A three-pronged lung signature consisting of decreased expression of lipid metabolism and coagulation genes and increased expression of proinflammatory cytokine genes had developed in mice that had

succumbed to infection, while a signature of increased expression of lipid metabolism and coagulation genes and lower expression of proinflammatory cytokine genes had developed in mice that recovered from infection [17].

Serous membranes support and protect the internal organs of all vertebrate animals. Each serous membrane consists of two layers separated by a thin, fluid-filled serosal cavity. The serosal cavity that envelops the lungs is called the pleural cavity, while the cavities that surround the abdominal organs and the heart are known as the peritoneal cavity and the pericardial cavity, respectively. Serosal cavities contain multiple immune cells including innate B cells and T cells, but macrophages are the dominant cell population. Serosal macrophages are divided into small macrophages and large macrophages based on their cell size and surface marker expression. Small serosal macrophages are MHCII^{+}F4/80^{-} and constitute ~10% of serosal macrophages while large serosal macrophages are MHCII^{-}F4/80^{+} and make up ~90% of serosal macrophages [18-20]. Serosal macrophages have been implicated in organ health. For example, postoperative gastrointestinal dysmotility can be ameliorated in mice by inhibiting peritoneal macrophage functions [21]. Furthermore, large peritoneal macrophages enter the liver to promote wound healing in mouse models of sterile liver damage and dextran sulfate sodium (DSS)-induced intestinal colitis [22, 23], while large pericardial macrophages enter the heart to improve immune responses after myocardial infarction [24]. However, small serosal macrophages have not been studied in diseases of the visceral organs, and serosal macrophages have never been studied in the context of viral infection.

In this manuscript, we use systems biology approaches as well as traditional “wet lab” techniques to identify a new lung macrophage population that originates in the pleural cavity and promotes recovery from influenza. To achieve this, we combined lung transcriptomic datasets to identify and confirm lung transcriptomic signatures that distinguish mild and severe influenza outcomes in mice. We then used a tissue deconvolution algorithm known as Digital Cell Quantifier (DCQ) to convert lung transcriptomic data into predictions of immune cell changes that preceded different disease outcomes [25]. We found that DCQ accurately predicted known cell population dynamics that occurred during influenza infection *in vivo*, and further predicted a lung cell population that transcriptionally resembled small serosal macrophages and whose numbers positively correlated with recovery from influenza.

We then used flow cytometry and microscopy to show that fluorescently-labeled PMs migrate from the pleural cavity into the lung after infection with A/California/04/2009 (Cal09) influenza virus after viral clearance has already occurred and recovery has been initiated. We further show that depleting PMs leads to increased virus-induced weight loss and a longer recovery time. In addition, depletion of PMs leads to increased inflammatory cytokines in the pleural cavity and increased neutrophil infiltration in the lung.

We are the first to show that PMs translocate to the lung during IAV infection and that they are important for the resolution of IAV-induced lung disease. Our study is also the first to propose a role for small serosal macrophages outside of the serosal cavities.

METHODS

Gene expression analysis

The primary transcriptomic data sets GEO Accession number GSE54048, GSE36328, GSE63786 and GSE33263 [17, 26-28] were extracted and quantile normalized using the “normalizeBetweenArrays” method available in the “limma” package of the R suite [29], and adjusted for batch effects using ComBat software [30]. Expression across each sample was normalized to the average expression of study- and time-matched mocks. Differential gene expression following viral infection was determined by deriving the ratio of expression between the average gene expression of influenza virus-infected replicates to the average of time-matched mock-infected samples applying a linear model fit using the “limma” package [29]. Criteria for differential expression (DE) were an absolute log-fold change of 2 and an adjusted *P* value of <0.05, calculated by Benjamini-Hochberg correction. Functional analysis of DE genes was done using Ingenuity Pathway Analysis (IPA; Ingenuity Systems) using a right-tailed Fisher exact test with a threshold of significance set at *P* value of 0.05.

Computational measurement of immune cell subsets

Immune cell dynamics during the course of infection were surveyed using the Digital Cell Quantifier (DCQ) algorithm as previously described [25]. Genome-wide gene expression was normalized for each infection relative to the average of the time-matched mock, and a log 2 transformation applied. Each gene expression entry was divided by the standard deviation across test samples. Analysis of relative cell quantity was run with three repeats and a lambda minimum of 0.2. For each of the 207 cell types in DCQ and

their three time points on day 1, day 3, and day 5, we used a simple linear model to estimate the relationship between the sample's expression for that cell type on that day to the weights on days 2, 4, 6, 8, 10, and 12.

Viruses

pH1N1 A/California/04/2009 and H1N1 A/Puerto Rico/8/1934 viruses were a kind gift from Dr. Adolfo García-Sastre (Icahn School of Medicine at Mount Sinai). Virus stocks were propagated in 8-day-old embryonated eggs (Charles River Laboratories) and titrated by plaque assays on MDCK cells.

Mouse experiments

All experiments with mice were performed in accordance with protocols approved by the University of California Riverside Institutional Animal Care and Use Committee. Female BALB/c mice, 8 to 12 weeks old, were purchased from Jackson Laboratory (Bar Harbor, ME) and used for all mouse experiments.

Mice were injected intrapleurally, under isoflurane anesthesia, with 100 μl of 10μM PKH26PCL fluorescent dye (Sigma Aldrich) one day before virus infection. In other experiments, mice were injected intrapleurally, under isoflurane anesthesia, with 50 μl of clodronate liposomes or PBS control liposomes (Encapsula Nano Sciences) one day before virus infection. Mice were challenged intranasally, under isoflurane anesthesia, with 50 μl PBS containing 10^2 or 10^4 PFU of pH1N1 A/California/04/2009 or H1N1 A/PR/8/1934 viruses, or mock challenged with PBS alone. Lungs were collected and

homogenized in 1 ml PBS and stored at −80 °C until virus titration. Viral titers were measured by plaque assays on MDCK cells.

Tissue homogenization

Lungs were harvested at indicated timepoints and washed in PBS before being placed in 2-ml tubes containing 1 ml 1X PBS, 3% FBS, and 1mM EDTA, and one ceramic bead (MP Biomedicals). Lung tissue was homogenized with the FastPrep-24 bead beater at 7.00 speed/s twice for 20 seconds each then placed on ice for 5 min and repeated. After homogenization, samples were centrifuged at 21,300xg for 15 min. Supernatant was aliquoted into new tubes and stored at -80°C.

Plaque assay

MDCK cells were seeded in 6-well culture plates and incubated at 37°C in 5% CO_2 for 24 hours. 10-fold serial dilutions were prepared in a solution containing 1x PBS, 0.21% BSA, 1% Pen/Strep, and 1% Ca/Mg. Cells were washed once with PBS before adding 200 ml of the serial dilutions. Plates were incubated at 37°C and were rocked side-to-side and forward-to-back every 15 minutes to distribute virus inoculum over the monolayer of cells for 1 hour. TPCK-treated trypsin (1 mg/ml) was added at a 1:1000 ratio to a supplemented 2X DMEM (2X DMEM, 2% Pen/Strep, 0.42% BSA, 20 mM HEPES, 0.24% $NaHCO_3$, 0.02% DEAE-Dextran) before mixing with 1.5% Oxoid Agar at a 1:1 ratio. 2 ml of the agar overlay was added to each well and allowed to cool for 15 min at room temperature before transferring to the 37°C incubator. Plates were incubated for 96 hours. After incubation, plates were fixed with 1 ml of a 3.7% formaldehyde solution and

incubated for 10 minutes to neutralize infectious virus. Overlay was flicked out with a spatula and stained for 20 min with crystal violet (0.095% crystal violet, 2.8% ethanol, 19% methanol). Plates were rinsed in tap water and plaques were counted to determine viral titers.

Cytokine and chemokine detection

Cytokines and chemokines from pleural fluid, serum, and lung were quantified using the LEGENDplex™ (Biolegend, 740150) mouse inflammation panel (13-plex). All samples were analyzed on a NovoCyte Quanteon and data was analyzed using LEGENDplex™ software (Biolegend).

Preparation of cell suspensions, flow cytometry and cell sorting

For isolation of pleural cavity cells, the pleural cavity was washed twice with 500 μl sterile cold PBS. The fluid was centrifuged at 500xg for 5 min at 4°C and resuspended in RBC lysis buffer (Sigma, R7757) for 5 min at room temperature. Fluorescence-activated cell sorting (FACS) buffer (1x PBS, 3% FBS and 2 mM EDTA) was added to stop the lysis and the fluid was centrifuged at 500xg for 5 min at 4°C and resuspended in FACS buffer.

For isolation of immune cells from blood, tubes were prepared with 1 ml of 4% sodium citrate. Blood was transferred to these tubes to prevent clotting and mixed well. 1 ml of FACS buffer was then added. Tubes were underlaid with 1 ml Histopaque (Sigma, 10771-6X100ML) using a Pasteur pipette. Samples were centrifuged at 400xg for 20 min at room temperature. The interface was collected and transferred to a new 15 ml conical

tube and washed with 10 ml of FACS buffer to remove Histopaque. After RBC lysis, samples were resuspended in FACS buffer.

For isolation of immune cells from lungs, lungs were removed and collected in a 15-ml centrifuge tube containing 10 ml FACS buffer and placed on ice. Lungs were transferred to a petri dish and macerated with razor blades. 3 ml of lung digestion buffer containing HBSS (Lonza, BE10-508F), 5% FBS, 1 mg/ml collagenase A (Sigma, 2674-500mg), and 0.05 mg/ml DNase I (Roche, 11284932001) was added and transferred to a new 15-ml centrifuge tube. Lungs were incubated at 37°C shaking for 1 hour. In the last 15 minutes of the digestion, lungs were syringed with a 1 ml syringe and 18g needle approximately 20 times. To stop digestion, 10 ml of FACS buffer was added and spun at 400xg for 4 min at 4°C. After lysing RBCs, cells were resuspended in FACS buffer and pushed through a 70-μm cell strainer.

Cavity cells, blood cells and lung single-cell suspensions were washed with PBS and resuspended in PBS containing live/dead fixable aqua dye (Invitrogen, L34957), and incubated at room temperature for 15 min. Cells were then washed and resuspended with FACS buffer. Fc receptors were blocked with anti-CD16/32 Fc block antibody (BD Biosciences, 553142) and Rat IgG then stained with primary antibodies. The antibodies used for staining were as follows: MerTK AF488 (BioLegend, 151504), CD115 PE-CF594 (Biolegend, 135528), I-A/I-E PerCP (BioLegend, 107624), Ly6c PE/Cy7 (BioLegend, 128018), CD64 APC (BioLegend, 139306), CD11b APC/Fire™ 750 (BioLegend, 101262), SiglecF BV421 (BD Biosciences, 565934), CD11c BV605 (117333), F4/80 BV650 (BioLegend, 123149), CD24 PE-CF594 (BD Biosciences, 562477), Ly6G PE (BioLegend, 127607), CD45 Alexa Fluor 700 (BioLegend, 103127). Cells were stained for 30 min at

4°C then washed with FACS buffer. Afterwards, the cells were fixed in 2% paraformaldehyde (PFA) for 20 min at 4°C and resuspended in FACS buffer. Samples were processed on an LSRII (BD Biosciences) or NovoCyte Quanteon (Agilent) and analyzed with FlowJo software (BD Biosciences). For cell sorting, samples were treated similarly, but without fixation, and sorted on a MoFlo Astrios EQ Cell Sorter (Beckman Coulter). FACS buffer used for cell sorting was HBSS without calcium or magnesium and supplemented with 3% FBS, 2mM EDTA and 25mM HEPES. Cells were dispensed into sorting buffer with 4x the amount of FBS.

Tissue preparation for immunofluorescence and hematoxylin and eosin staining

Mice were sacrificed at the indicated time points. Lungs were inflated with 1 ml of a solution containing 1 part 4% PFA/30% sucrose and 2 parts of optimal cutting temperature compound (OCT) media (Fisher Scientific). Inflated lungs were tied off and stored in 4% PFA/30% sucrose at 4°C overnight. The following day lungs were transferred to 30% sucrose and stored overnight at 4°C. Lungs were then blocked in OCT on dry ice and stored at -80°C. Tissue was sectioned at 10-20 μm on a cryostat. For histological assessment tissues were stained with hematoxylin and eosin. Slides were assessed in a double-blind manner.

For immunofluorescence, slides were mounted with ProLong Glass Antifade Mountant with NucBlue (Invitrogen, P36981). Images were acquired using a Keyence BZ-X710 fluorescent microscope. Image analysis was conducted with two images per section, two sections per slide, two slides per animal with n = 5 animals per condition. Images were analyzed on ImageJ.

Ex vivo labeling of macrophages with PKH26PCL dye

Sorted cell populations were washed twice with serum-free media then resuspended in 500 μl diluent from the PKH26PCL-1KT. In a separate tube, PKH dye solution was prepared at a 5μM concentration in 500 μl of PKH dye. Dye solution was then added to resuspended cells and incubated for 5 minutes and then washed three times with media containing serum.

Statistical analysis

All results were presented as the mean ± SEM. R and Excel were used for statistical analyses. The analyses were conducted using Student's t test for comparison between two groups and one-way ANOVA was used to test comparisons between multiple groups (*$P < 0.05$, **$P < 0.01$, ***$P < 0.001$, ****$P < 0.0001$, and ns for not significant).

RESULTS

Host response differences in expression of inflammatory, metabolic, cell cycle and tissue repair genes distinguish influenza disease outcomes.

Previously, we identified a gene expression signature in the mouse lung that distinguished between severe and mild influenza [17]. We sought to expand our gene expression analysis to a wider range of influenza disease outcomes by including intermediate disease outcomes such as moderate weight loss and severe weight loss with subsequent recovery. Therefore, we integrated transcriptional data from our study [17] with data from an independent study of similar design [26]. A description of the two studies and their combined weight loss outcomes are shown (**Figures 1A and 1B**). We restricted our analysis to those differentially-expressed (DE) genes that had a log fold change of 2 or more with an adjusted p-value cut-off of 0.05. When DE genes were clustered based on their biweight midcorrelation (bicor) across samples, six gene expression modules were identified and assigned unique colors (**Figure 1C**). We then used Ingenuity Pathway analysis (IPA) to assign functional categories to the genes within each module. The red module was enriched for genes in inflammation-associated pathways such as “Granulocyte adhesion and diapedesis” and “Crosstalk between dendritic cells and natural killer cells”. The increased induction of red module transcripts was associated with increased weight loss. The orange module, which had a unique expression pattern, was enriched for genes involved in lipid metabolism (“LXR/RXR activation” and “FXR/RXR activation” pathways) and coagulation. Upregulation of genes in this module on any day post infection was associated with survival. Thus, the expression patterns of genes within the red and orange modules support our previous

observation of perturbations in inflammation, lipid metabolism, and coagulation signaling gene expression.

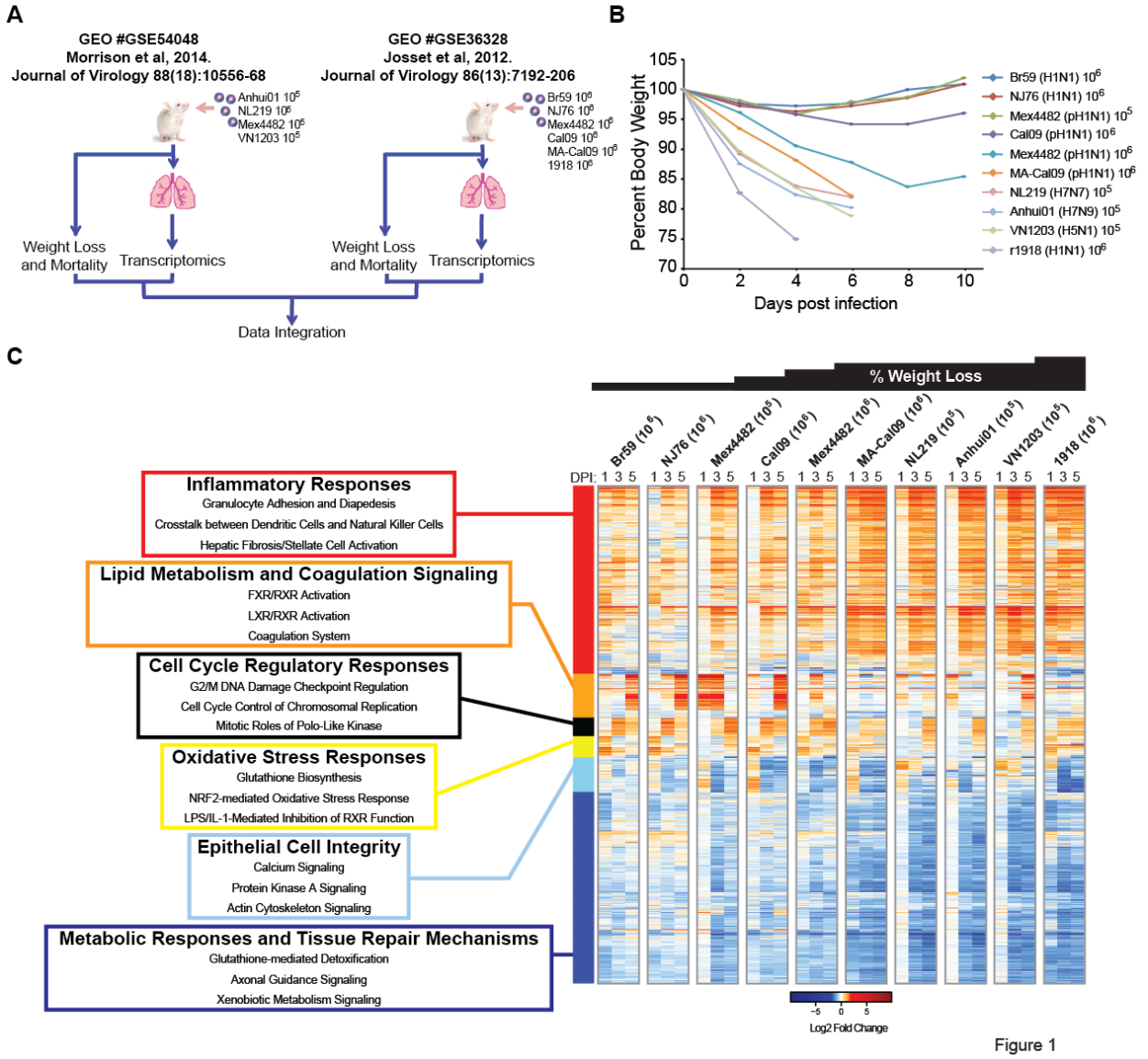

Figure 1. Different influenza disease outcomes are distinguished by host response differences in expression of inflammatory, metabolic, cell cycle and tissue repair genes. (A) Schematic showing the integration of BALB/C mouse data from GSE54048 and GSE36328. Experimental data were combined to produce (B) a combined weight loss dataset and a combined transcriptional dataset. (C) Hierarchical clustering of differential gene expression in murine lungs infected with influenza virus. Biweight midcorrelation clustering of 6012 genes that were found to be differentially expressed in any one condition (infection and time). Heatmap represents average gene expression intensity. Genes shown in red were upregulated and genes shown in blue were downregulated relative to uninfected lungs.

We then characterized the genes in the other four expression modules. The yellow module, which contained genes involved in oxidative stress responses, did not have an obvious pattern that related to weight loss or mortality. The sky-blue module, which contained calcium and actin cytoskeleton signaling genes, also lacked a pattern with regards to weight loss and mortality. The downregulation of genes in the dark-blue module, which was enriched for cell cycle and metabolic response genes, was associated with increased weight loss. Strikingly, expression of black module genes above a certain threshold on any day post infection was associated with survival. The black module contained mitosis and cell cycle control genes. We hypothesized that this signature resulted from differential activation or infiltration of immune cells in the lungs of mice that recovered versus those that succumbed to influenza infection.

Several immune cell types are predicted to correlate with influenza disease severity.

To explore the immune cell populations that were potentially associated with the weight loss and mortality outcomes, we employed a tissue deconvolution method known as DCQ. The DCQ algorithm compares the gene expression profiles from 207 different immune cells with whole organ transcriptional data to predict the quantities of immune cells within a complex organ [25]. This method utilizes a panel of genes encoding cell surface markers that are commonly used for flow cytometry, and whose transcript and protein levels are concordant [25]. We took the populations measured by DCQ and used linear regression to identify the cell populations whose numbers were most highly

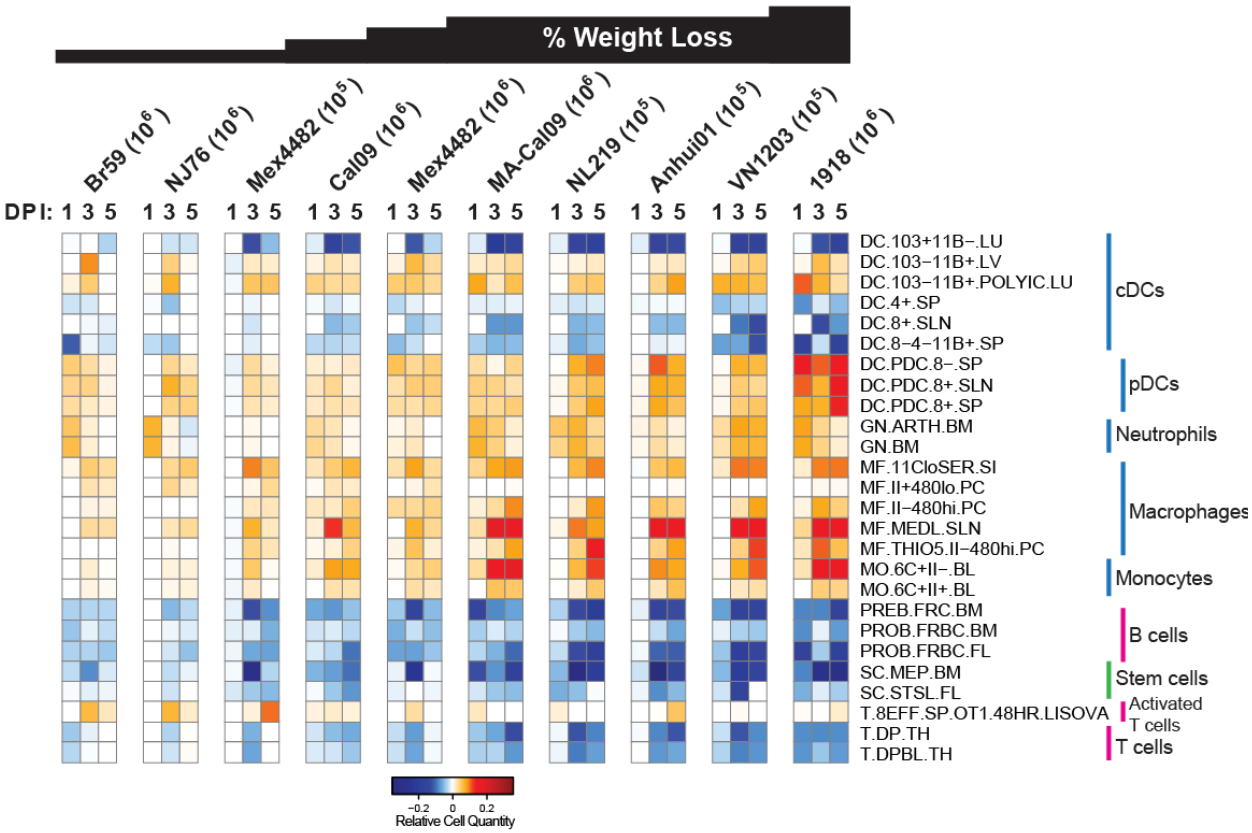

Figure 2. Digital cell quantifier identified immune cell subsets that predict disease severity or recovery across independent experiments. We surveyed the *in vivo* dynamics across time and viral strains using digital cell quantifier (DCQ; http://dcq.tau.ac.il). Linear regression models revealed distinct immune cell populations predicted to drive disease morbidity as defined by weight loss following influenza virus infection. The heatmap represents the relative quantity of cell types with significant relationships ($p < 0.05$) between that cell type on at least one day to the weights on at least one day after filtering for observations where data for at least 8 samples were available.

associated with weight loss in infected animals. We identified 26 cell types that were positively or negatively correlated with influenza disease outcomes (**Figure 2**). Loss of stem cell populations as well as lymphoid cells such as immature B and T cells and effector $CD8^+$ T cells was associated with increased weight loss. An increase in monocytes, plasmacytoid dendritic cells (pDCs) and granulocytes was associated with increased weight loss. Though increases in several conventional dendritic cell (cDC) and MF populations were associated with increased weight loss and death, the presence of other cDC and MF populations were associated with mild disease and recovery. For

example, decreases in CD103-positive cDCs (DC.103^{+}11B^{-}.LU) were associated with increased morbidity and mortality. The presence of cells resembling MHCII^{+}F4/80^{lo} peritoneal MFs (MF.II^{+}480^{lo}.PC) were associated with mild disease.

Immune cell predictions are conserved across multiple transcriptomic datasets.

To further validate the DCQ predictions, we subjected two additional microarray datasets to DCQ. In Shoemaker et al. (GSE63786), C57BL/6 mice were infected with 10^5 PFU of Cal09 or VN1203, and monitored over the course of 7 days [27] (**Figure S1A**). Lungs from VN1203-infected mice were found to have higher viral loads and more pathology than lungs from Cal09-infected mice [27]. In McDermott et al. (GSE33263), C57BL/6 mice were infected with 10^2, 10^3 or 10^4 PFU VN1203 [28] (**Figure S1B**). Higher inoculation titers led to increased weight loss and mortality [28]. When GSE63786 and GSE33263 were run through the DCQ algorithm, we found that the 26 cell types identified from the BALB/c datasets (**Figure 2**) largely showed a similar pattern in the C57BL/6 data (**Figures S1C and S1D**). As with the BALB/c mice, an increase in monocytes and granulocytes was associated with increased tissue pathology and weight loss in C57BL/6 mice (**Figures S1C and S1D**). Loss of stem cell populations, immature B and T cells and effector CD8^{+} T cells was also associated with increased weight loss. Again, the presence of cells resembling MHCII^{+}F4/80^{lo} peritoneal macrophages were associated with mild disease (**Figures S1C and S1D**). The only prediction that did not hold across the 4 datasets was that for pDC populations. Higher pDC numbers were associated with severe disease in BALB/c mice (**Figure 2**), but were associated with mild disease in C57BL/6 mice (**Figure S1**).

Flow cytometry validates DCQ predictions.

DCQ accurately identified cell population dynamics that have been shown to occur during influenza infection *in vivo* (**Figures 2** and **S1**). For instance, $CD103^{+}CD11b^{-}$ dendritic cell numbers decrease post infection, modeling what occurs *in vivo* when they exit the lung and traffic to the draining lymph nodes to present antigen to $CD8^{+}$ T cells [31, 32].

To further emphasize the value of our approach, we conducted *in vivo* experiments to confirm some of the predictions. BALB/c mice were infected intranasally with 10^4 pH1N1 A/California/09 (Cal09) virus to induce mild disease or 10^4 H1N1 A/Puerto Rico/1934 (PR8) virus to induce severe disease. Control mice received PBS intranasally. We isolated, stained, and subjected lung cells to flow cytometry on day 3 post infection. We validated the prediction that more neutrophils and $Ly6C^{+}$ monocytes were recruited to the lung during severe disease (**Figure S2**).

Influenza virus infection promotes the recruitment of pleural macrophages to the lung.

Our data thus far supported the idea of a $MHCII^{+}F4/80^{lo}$ macrophage population that originates in a serosal cavity and is present in the lungs of mice that recover from influenza. Since the macrophage populations of the pleural and peritoneal cavities are analogous [18, 20], and the pleural cavity envelopes the lung, we hypothesized that the $MHCII^{+}F4/80^{lo}$ lung macrophages predicted by DCQ originated in the pleural cavity. Though CD11b, CD115, F4/80 and MHCII are sufficient for distinguishing the two pleural

macrophage (PM) populations, these markers are insufficient for distinguishing the various macrophage populations in the lung. To circumvent issues with lung macrophage identification, we focused instead on the potential origin of the novel lung population. PMs

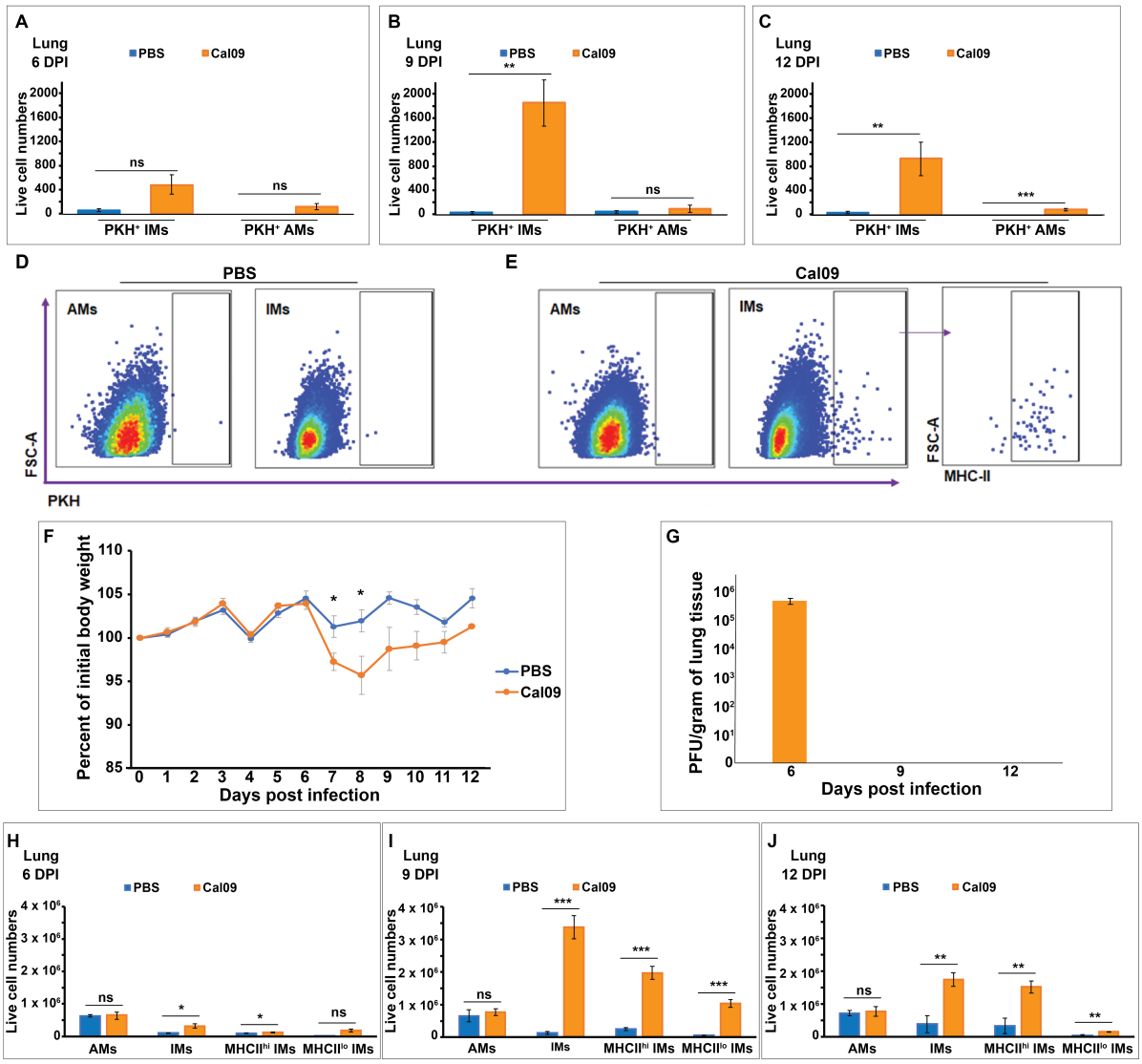

Figure 3. Influenza virus infection promotes the recruitment of pleural macrophages to the lung. BALB/c mice were intrapleurally injected with PKH26PCL dye one day before they were intranasally infected with 10^2 Cal09 virus or mock-infected with PBS as a control. (A-C) Quantification of live cell numbers of PKH$^+$ AMs and IMs in Cal09- or mock-infected mice. (D) Representative flow plots of PBS control mice. (E) Representative flow plots of Cal09 infected mice. (F) Representative growth curve of Cal09-infected versus PBS control mice. (G) Virus titers from lungs of mice in (F). (H-J) Quantification of live cell numbers of AMs and IMs in Cal09- or mock-infected mice. Data shown as mean ± SEM (n=4 from each group, *P<0.05, **P<0.01, ***P<0.001, Student's t-test). AM = alveolar macrophage (MerTK$^+$CD64$^+$SiglecF$^+$CD11b$^-$); IM = interstitial macrophage (MerTK$^+$CD64$^+$CD11b$^+$SiglecF$^-$).

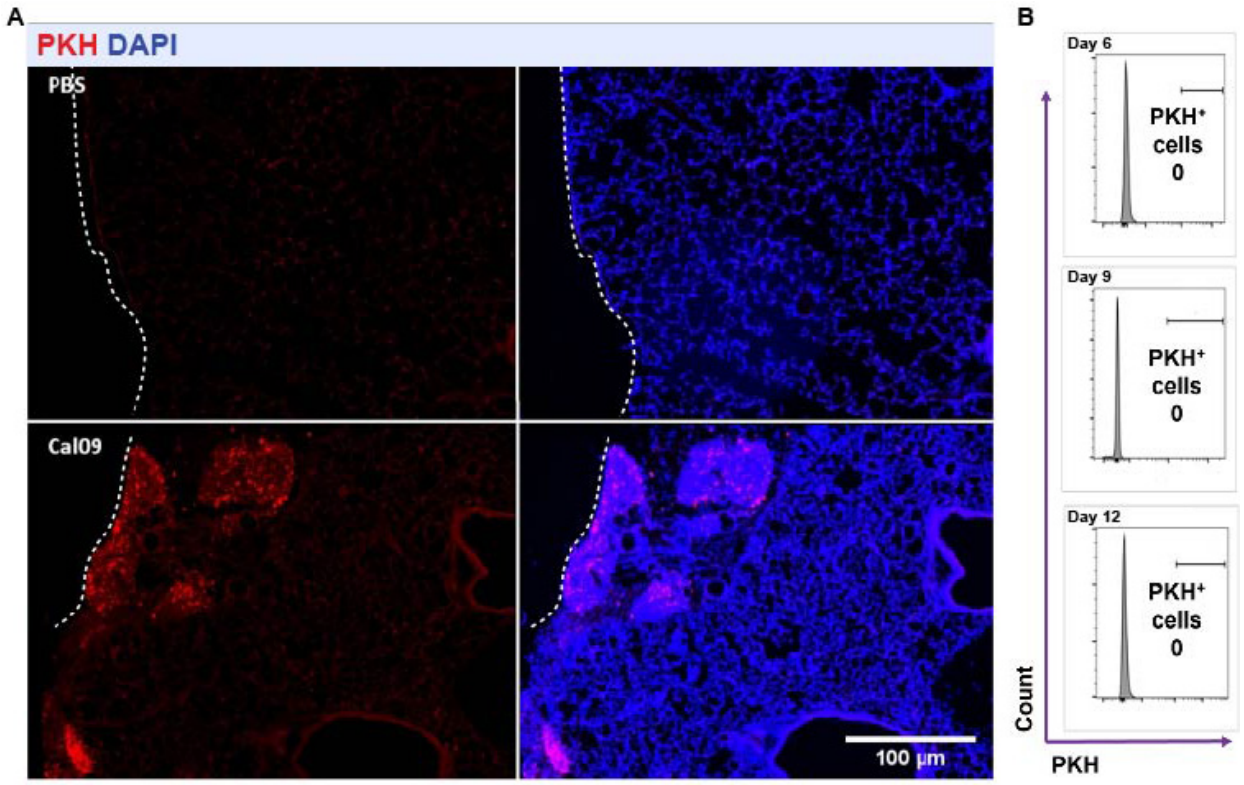

Figure 4. PMs localize near the mesothelium. (A) Representative fluorescent images of BALB/c naïve and Cal09-infected lungs harvested 9 days post infection. PMs were labeled *in vivo* with PKH26PCL dye (red) and counterstained with DAPI (blue). The mesothelium is depicted by the white dotted line (n = 3-7 from each group). (B) Flow cytometry of blood harvested from mice that had been intrapleurally injected with PKH26PCL dye then infected with Cal09 on days 6, 9 and 12 post infection.

were labeled *in vivo* by injecting a red phagocyte-specific dye (PKH26PCL) into the pleural cavities of mice 1 day prior to infection. When mice were infected intranasally with 10^2 PFU of Cal09, PKH26PCL-labelled cells accumulated in the lung (**Figure 3**). Translocated PMs were detected in the lungs on days 6, 9, and 12 post infection, but more accumulation of the PKH^+ PMs occurred on 9 and 12 days post infection when compared to the uninfected controls (**Figures 3A-E**). Flow cytometry gating strategies to distinguish pleural and lung macrophage subpopulations are outlined in **Figures S3** and **S4**.

PKH$^+$ cells in the lung were CD64$^+$MerTK$^+$SiglecF$^-$CD11b$^+$ which are phenotypically like interstitial macrophages (IMs) (**Figure 3E**). Heterogeneity amongst IMs has been researched in multiple studies [33-35]. One way of distinguishing them is based on their expression on MHCII. We found that the PKH$^+$ lung cells resembled MHCII$^+$ IMs (**Figure 3E).** Accumulation of this MHCII$^+$CD64$^+$Mertk$^+$SiglecF$^-$CD11b$^+$ population that had originated in the pleural cavity only occurred once animals began to regain weight and after they had cleared virus from their lungs (**Figures 3F-G**). We also observed an overall increase in the total number of IMs in the lung during IAV infection (**Figures 3H-J**).

To establish the location of the PKH$^+$ PMs in the lung, frozen lung sections were immunostained and imaged by fluorescence microscopy 9 days post infection (**Figure 4A**). PKH$^+$ PMs in the lung are detected near the mesothelium (shown by the white dotted line) and within regions of dense DAPI signal (**Figure 4A).** No PKH$^+$ PMs were detected in the PBS mock-infected control group. In addition, flow cytometric analysis of immune cells isolated from blood on days 6, 9, and 12 post infection showed no PKH$^+$ PMs in either the infected or the control group (**Figure 4B)**.

Pleural macrophage depletion leads to increased weight loss and slower recovery from IAV infection.

Previous studies have shown conflicting evidence for a role of cavity macrophages in models of liver, heart and intestinal injury, showcasing differences in recruitment, wound repair, and weight loss [22-24, 36]. Another study suggested a role for PMs in bacterial clearance in bacterial pneumonia [37]. However, no study to date has

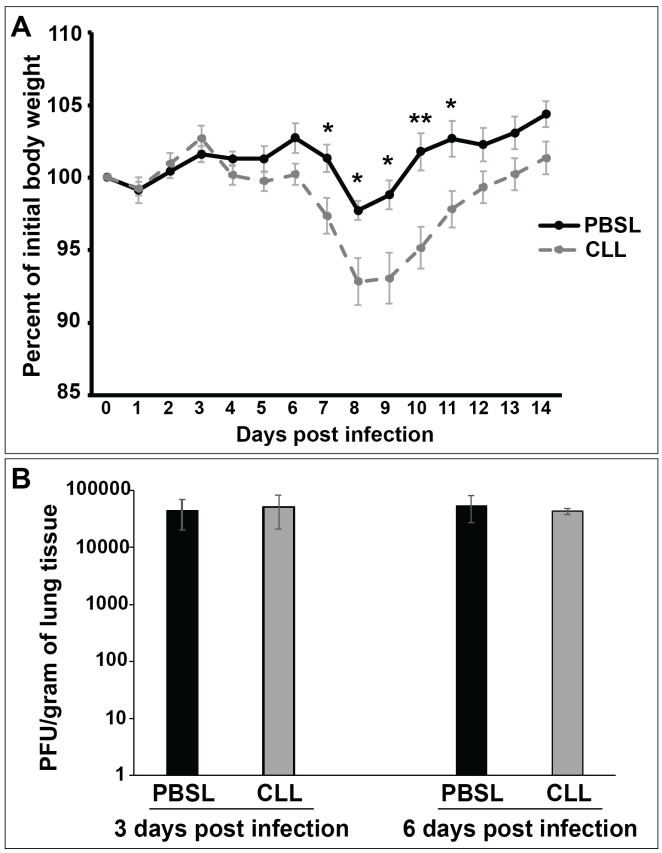

Figure 5. PM depletion increases disease severity without impacting viral titers. BALB/c mice received an intrapleural injection of CLL or PBSL one day before infection with 10^2 PFU of Cal09. (A) Weight loss tracked over 14 days post infection in both CLL-injected and PBSL-injected groups (n=10 per group). (B) Virus titers from lungs of mice (n=3 per group). Data shown as mean ± SEM (*P<0.05, **P<0.01, ***P<0.001, ****P<0.0001, Student's t-test).

investigated the role of PMs in viral infection. To test whether PMs affect influenza outcomes, we depleted PMs by injecting clodronate liposomes (CLL) into the pleural cavities of mice 1 day prior to infection with Cal09 virus. Flow cytometry confirmed PMs were depleted 24 hours after injection (**Figure S5**), and up to 14 days after injection. PM-depleted mice lost more weight compared to the PBS liposomes (PBSL)-injected control mice (**Figure 5A**). However, we noted no statistical differences in H&E-stained lungs (**Figure S6A**) that had been scored for airway thickening, alveolar destruction, and vascular inflammation (**Figure S6B**). Lungs viral loads were unaffected by PM depletion (**Figure 5D**).

Since PM depletion led to more IAV-induced weight loss, we asked whether we would see increased inflammation in the lungs of PM-depleted mice. By measuring the number of $CD45^+$ cells in the lung, we found that the number of total leukocytes in the lungs of PM-deficient and PM-sufficient mice were the same (**Figure 6A**). However, when

we looked at individual leukocyte populations, we found that CLL-treated mice had a significantly higher percentage of neutrophils than PBSL-treated mice did on day 9 post infection (**Figure 6B**). Additionally, on day 9 post infection, PM depletion led to increased pleural cavity inflammation indicated by increased proinflammatory cytokines: interferon-gamma (IFN-γ), tumor necrosis factor alpha (TNF-α) and monocyte chemoattractant protein-1 (MCP-1) (**Figure 6C**). However, no proinflammatory cytokines were increased in the lung between the infected groups (**Figure 6D**), though PM-depletion caused an increase in serum IFN-γ levels in response to lung IAV infection.

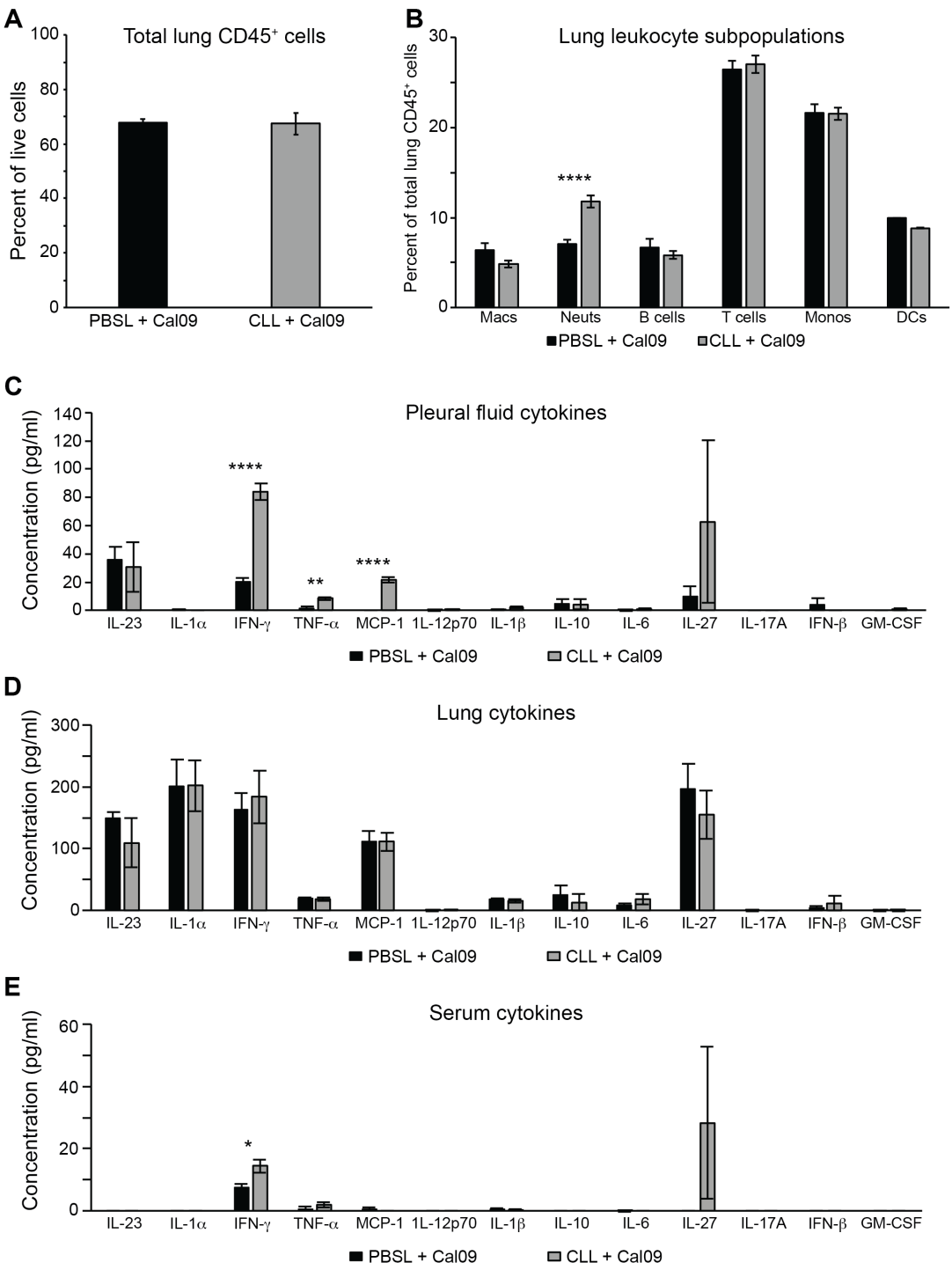

Figure 6. PM depletion increases pleural cavity inflammatory cytokines and infiltration of neutrophils in the lung on 9-days post-infection. (A) Flow cytometric analysis of lung leukocytes ($CD45^+$), (B) *left to right*, macrophages ($CD64^+Mertk^+$), neutrophils ($Ly6G^+CD11b^+$), B cells ($CD11c^-CD11b^-Ly6G^-CD24^+MHC\text{-}II^+$), T cells ($CD11c^-CD11b^-Ly6G^-CD24^-MHC\text{-}II^-$), monocytes ($CD11b^+Ly6C^{lo/hi}$), DCs ($CD11c^+CD11b^{lo/hi}CD24^+MHC\text{-}II^+$). Cytokines from (C) pleural fluid, (D) lung homogenate, and (E) serum. Data shown as mean ± SEM (n=5 from each group, *P<0.05, **P<0.01, ***P<0.001, ****P<0.0001, Student's t-test). Macs = macrophages, neuts = neutrophils, monos = monocytes, DCs = dendritic cells

Both small and large PM populations can translocate to the lung after IAV infection.

Other studies have focused on the roles that large serosal macrophage migration from the pleural, pericardial and peritoneal cavities play in the health of the organs they envelop [22-24, 37]. None to date, have tested whether small serosal macrophages have the capacity to translocate to the visceral organs. As our initial DCQ prediction implicated small serosal macrophages in recovery from influenza, we designed an experiment to test which PM subpopulation could migrate into the lung by intrapleurally transferring labeled SPMs or LPMs into naïve mice one day prior to IAV infection (**Figure 7A**). SPMs and LPMs were isolated from BALB/c mice using fluorescently-activated cell sorting (FACS) and stained *ex vivo* with PKH26PCL. Because we harvest 10-fold less SPMs than LPMs from the pleural cavity of each donor mouse, we could not provide equal amounts of each subpopulation. Instead, we injected 200,000 PKH-labeled LPMs or 50,000 PKH-labeled SPMs into the pleural cavities of each mouse one day before mock infection with PBS or infection with Cal09. PKH26PCL-labelled cells from both SPM and LPM transfers were detected in the lungs of IAV-infected mice 9 days post infection, but not in the mock-infected group (**Figure 7B**). Quantification of the PKH^+ lung cells showed there was no difference between the percentage of PKH^+ lung macrophages that accumulated whether SPMs or LPMs were the transferred population even though 4-fold less PKH-labelled SPMs than LPMs had been transferred into the pleural cavities of the mice prior to infection suggesting that SPMs are more migratory (**Figure 7**).

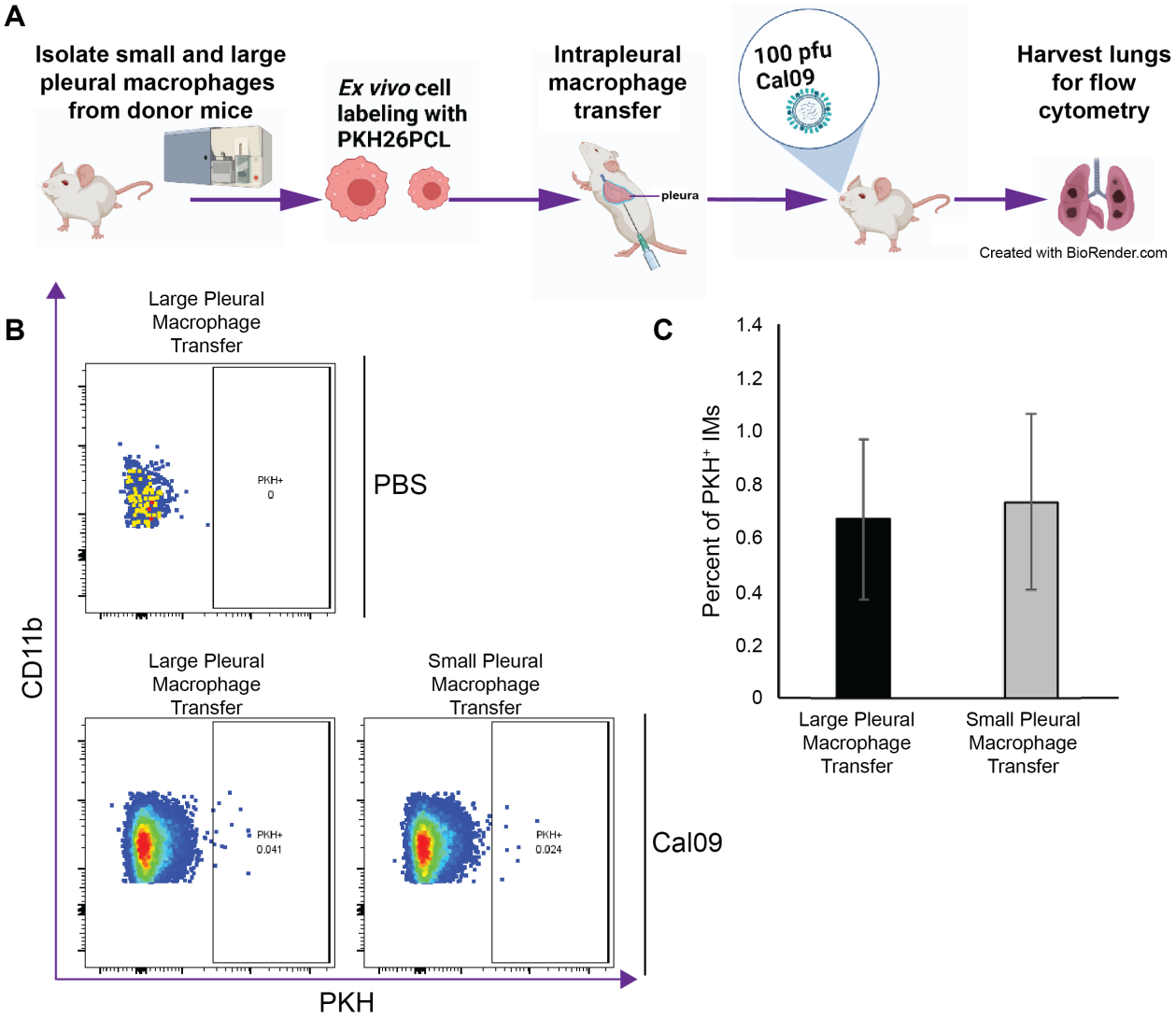

Figure 7. SPMs and LPMs are recruited to the lung after IAV infection
(A) Schematic figure showing experimental strategy. (B) Representative flow plots of mouse lungs from SPM and LPM transfers. (C) Quantification of PKH$^+$ IMs in lungs from Cal09-infected mice. Data shown as mean ± SEM (n=4 from each group, *P<0.05, **P<0.01, ***P<0.001, ****P<0.0001, Student's t-test)

DISCUSSION

An important feature of our study was the use of systems biology approaches to generate hypotheses. By combining lung transcriptomic data from two IAV infection studies, we were able to identify signatures that could distinguish mild and severe disease outcomes in mice. We were then able to use DCQ and linear regression to discover immune populations in the ImmGen database that could be driving the lung transcriptomic signatures. There is a great deal of heterogeneity amongst lung macrophage populations [19, 20, 33-35, 38]. However, DCQ accurately predicted the presence of a population resembling small peritoneal macrophages that accumulated after IAV infection and only in animals that survived IAV infection. This prediction was foundational and served as an important tool for identifying a novel immune cell population in our system. Nevertheless, there are caveats to tissue deconvolution approaches. Many macrophage populations from different organs share similar phenotypic markers which make it difficult to predict the origin of immune cell populations. In our case, the uniqueness of the small peritoneal macrophage transcriptome in ImmGen was an asset to our predictions and subsequent analyses. As such, characterizing additional immune populations of the serosal cavities and other unique niches would be useful for future predictions.

IAV-induced lung injury triggers the recruitment of mature macrophages across the mesothelium. This was observed through our labeling of pleural macrophages via intrapleural injection of PKH26PCL before infection and detected by flow cytometry and immunofluorescence (**Figures 3** and **4**). A recent study defined one population of IMs as nerve- and airway-associated macrophages (NAMs) that proliferate rapidly after IAV infection and highly express MHCII genes [39]. Interestingly, our data also show a robust

increase in the numbers of IMs, most of which were an MHCII^{hi} subpopulation that peaked at 9-days post-infection. In our model of IAV infection, once PMs translocate to the lung, they contribute to the IM pool and phenotypically resemble MHCII^{hi} IMs (**Figure 3**). However, unlike with NAM depletion [39], PM depletion had no effect on monocyte recruitment (**Figure 6B**).

Perhaps it is because small serosal macrophages constitute ~10% of serosal macrophages or because they possess qualities that are atypical when compared to other tissue resident macrophages [19, 40, 41], but they are poorly studied when compared to their larger counterparts. Other studies have shown rapid migration of GATA6^{+} large serosal macrophages. However, these studies focused more on sterile injury or inflammation of the liver, heart, and intestine [22-24]. In our study, the IAV infection model provides a different context where PMs are recruited at a much later time point after the resolution of viral infection and when restoration of homeostasis is critical. The immune response to IAV infection is a delicate balance of efficient viral clearance followed by tissue regeneration. In other studies, cavity-organ recruitment relied on CD44 and the damage-associated molecular pattern (DAMP), ATP, serving as a local “touch me” signal [22, 23, 42]. We did not investigate whether our PM populations relied on a similar mechanism. However, our research expands on those studies by showing that SPMs can migrate to the lung (**Figure 7**).

The pleural cavity may serve as a reservoir for other immune cells that can migrate to the lung. B1a cells, another pleural cavity immune cell population, have important roles in bacterial pneumonia and were suggested to migrate to the lung [43]. Furthermore, during IAV infection, pleural cavity B1a cells have important pulmonary responses by

infiltrating infected lungs [44]. Whether other pleural cavity cell populations can migrate to the lung has not been identified. However, PKH26PCL is a phagocytic dye and no other PKH^+ cells were identified within the lungs. Therefore, it is unlikely that monocytes, dendritic cells, or granulocytes migrate to the lung from the pleural cavity.

A recent study using genetic fate-mapping techniques showed only surface accumulation of pleural and peritoneal macrophages after organ injury and found no role for them in tissue repair or regeneration [36]. However, our results indicate otherwise. We visualized PM translocation at later timepoints--during the resolution phase--of a seasonal IAV infection model and show that PMs affect disease severity. PM ablation leads to increased weight loss and neutrophil influx in the lungs of IAV-infected mice. While we were preparing this manuscript, a paper describing increased bacterial burden and mortality upon PM depletion in a mouse model of bacterial pneumonia was published [37]. Unlike Bénard et al., where bacterial burdens increased upon PM depletion and resulted in increased mortality, we saw increased disease severity without differences in viral titers between PM-depleted and control groups after IAV infection. Additionally, we found that PMs traffic to the lung after IAV infection, while they did not test for PM translocation.

PMs are important immunomodulators that impact the recovery of IAV-infected mice by decreasing lung neutrophil infiltration and decreasing pleural space inflammation (**Figure 6**). Tissue resident macrophages can “cloak” proinflammatory debris to contain neutrophil-driven tissue damage and inflammation [45]. It is feasible that recruited PMs may play a role in “cloaking” damage signals to prevent neutrophil infiltration. Pulmonary inflammation can lead to pleural inflammation, which is associated with increased

mortality in pneumonia patients and in patients hospitalized with pleural effusion [46, 47]. IFN-γ levels were higher in both pleural fluid and serum of IAV-infected PM-depleted mice. Lack of IFN-γ has been shown to decrease susceptibility to lethal infection by increasing activation of group II innate lymphoid cells (ILC2s) [48]. Following viral infection, patients are left more vulnerable to subsequent pneumonia, and the PMs may limit inflammation after infection and decrease susceptibility to pneumonia. Altogether, we show that PMs migrate to the lung during IAV infection and play a role in limiting disease severity by modulating inflammatory responses both in the pleural cavity and in the lung. Selectively targeting PMs could serve as a strategy for treating severe influenza and other lung and pleural diseases. Future studies to understand how PM translocation and plasticity are regulated are warranted.

ACKNOWLEDGEMENTS

We thank Dr. Maudry Laurent-Rolle for critical feedback on this manuscript. We thank Dr. Adolfo García-Sastre for kindly providing pH1N1 A/California/04/2009 and H1N1 A/Puerto Rico/8/1934 influenza viruses as well as MDCK cells.

FUNDING SOURCES

This research was supported by University of California, Riverside funds (to JM) and a Regents Faculty Fellowship, University of California (to JM).

CONFLICTS OF INTEREST

The authors have declared that no conflict of interest exists.

REFERENCES

1. Horimoto, T. and Y. Kawaoka, *Influenza: lessons from past pandemics, warnings from current incidents.* Nat Rev Microbiol, 2005. **3**(8): p. 591-600.
2. Lamichhane, P.P. and A.E. Samarasinghe, *The Role of Innate Leukocytes during Influenza Virus Infection.* J Immunol Res, 2019. **2019**: p. 8028725.
3. Kash, J.C., et al., *Genomic analysis of increased host immune and cell death responses induced by 1918 influenza virus.* Nature, 2006. **443**(7111): p. 578-81.
4. Perrone, L.A., et al., *H5N1 and 1918 pandemic influenza virus infection results in early and excessive infiltration of macrophages and neutrophils in the lungs of mice.* PLoS Pathog, 2008. **4**(8): p. e1000115.
5. Short, K.R., et al., *Pathogenesis of influenza-induced acute respiratory distress syndrome.* Lancet Infect Dis, 2014. **14**(1): p. 57-69.
6. Tisoncik, J.R., et al., *Into the eye of the cytokine storm.* Microbiol Mol Biol Rev, 2012. **76**(1): p. 16-32.
7. Writing Committee of the, W.H.O.C.o.C.A.o.P.I., et al., *Clinical aspects of pandemic 2009 influenza A (H1N1) virus infection.* N Engl J Med, 2010. **362**(18): p. 1708-19.
8. Herold, S., et al., *Influenza virus-induced lung injury: pathogenesis and implications for treatment.* Eur Respir J, 2015. **45**(5): p. 1463-78.
9. Cole, S.L., et al., *M1-like monocytes are a major immunological determinant of severity in previously healthy adults with life-threatening influenza.* JCI Insight, 2017. **2**(7): p. e91868.
10. Chi, Y., et al., *Cytokine and chemokine levels in patients infected with the novel avian influenza A (H7N9) virus in China.* J Infect Dis, 2013. **208**(12): p. 1962-7.
11. de Jong, M.D., et al., *Fatal outcome of human influenza A (H5N1) is associated with high viral load and hypercytokinemia.* Nat Med, 2006. **12**(10): p. 1203-7.
12. Wang, Z., et al., *Early hypercytokinemia is associated with interferon-induced transmembrane protein-3 dysfunction and predictive of fatal H7N9 infection.* Proc Natl Acad Sci U S A, 2014. **111**(2): p. 769-74.
13. Fukushi, M., et al., *Serial histopathological examination of the lungs of mice infected with influenza A virus PR8 strain.* PLoS One, 2011. **6**(6): p. e21207.
14. Narasaraju, T., et al., *Excessive neutrophils and neutrophil extracellular traps contribute to acute lung injury of influenza pneumonitis.* Am J Pathol, 2011. **179**(1): p. 199-210.
15. Traylor, Z.P., F. Aeffner, and I.C. Davis, *Influenza A H1N1 induces declines in alveolar gas exchange in mice consistent with rapid post-infection progression from acute lung injury to ARDS.* Influenza Other Respir Viruses, 2013. **7**(3): p. 472-9.
16. Xu, T., et al., *Acute respiratory distress syndrome induced by avian influenza A (H5N1) virus in mice.* Am J Respir Crit Care Med, 2006. **174**(9): p. 1011-7.
17. Morrison, J., et al., *H7N9 and other pathogenic avian influenza viruses elicit a three-pronged transcriptomic signature that is reminiscent of 1918 influenza virus and is associated with lethal outcome in mice.* J Virol, 2014. **88**(18): p. 10556-68.
18. Bain, C.C., et al., *Long-lived self-renewing bone marrow-derived macrophages displace embryo-derived cells to inhabit adult serous cavities.* Nat Commun, 2016. **7**: p. ncomms11852.

19. Ghosn, E.E., et al., *Two physically, functionally, and developmentally distinct peritoneal macrophage subsets.* Proc Natl Acad Sci U S A, 2010. **107**(6): p. 2568-73.
20. Kim, K.W., et al., *MHC II+ resident peritoneal and pleural macrophages rely on IRF4 for development from circulating monocytes.* J Exp Med, 2016. **213**(10): p. 1951-9.
21. Maehara, T., et al., *Therapeutic action of 5-HT3 receptor antagonists targeting peritoneal macrophages in post-operative ileus.* Br J Pharmacol, 2015. **172**(4): p. 1136-47.
22. Honda, M., et al., *Directly recruited GATA6 + peritoneal cavity macrophages contribute to the repair of intestinal serosal injury.* Nat Commun, 2021. **12**(1): p. 7294.
23. Wang, J. and P. Kubes, *A Reservoir of Mature Cavity Macrophages that Can Rapidly Invade Visceral Organs to Affect Tissue Repair.* Cell, 2016. **165**(3): p. 668-78.
24. Deniset, J.F., et al., *Gata6(+) Pericardial Cavity Macrophages Relocate to the Injured Heart and Prevent Cardiac Fibrosis.* Immunity, 2019. **51**(1): p. 131-140 e5.
25. Altboum, Z., et al., *Digital cell quantification identifies global immune cell dynamics during influenza infection.* Mol Syst Biol, 2014. **10**: p. 720.
26. Josset, L., et al., *Implication of inflammatory macrophages, nuclear receptors, and interferon regulatory factors in increased virulence of pandemic 2009 H1N1 influenza A virus after host adaptation.* J Virol, 2012. **86**(13): p. 7192-206.
27. Shoemaker, J.E., et al., *An Ultrasensitive Mechanism Regulates Influenza Virus-Induced Inflammation.* PLoS Pathog, 2015. **11**(6): p. e1004856.
28. McDermott, J.E., et al., *Conserved host response to highly pathogenic avian influenza virus infection in human cell culture, mouse and macaque model systems.* BMC Syst Biol, 2011. **5**: p. 190.
29. Ritchie, M.E., et al., *limma powers differential expression analyses for RNA-sequencing and microarray studies.* Nucleic Acids Res, 2015. **43**(7): p. e47.
30. Johnson, W.E., C. Li, and A. Rabinovic, *Adjusting batch effects in microarray expression data using empirical Bayes methods.* Biostatistics, 2007. **8**(1): p. 118-27.
31. Ballesteros-Tato, A., et al., *Temporal changes in dendritic cell subsets, cross-priming and costimulation via CD70 control CD8(+) T cell responses to influenza.* Nat Immunol, 2010. **11**(3): p. 216-24.
32. Helft, J., et al., *Cross-presenting CD103+ dendritic cells are protected from influenza virus infection.* J Clin Invest, 2012. **122**(11): p. 4037-47.
33. Chakarov, S., et al., *Two distinct interstitial macrophage populations coexist across tissues in specific subtissular niches.* Science, 2019. **363**(6432).
34. Gibbings, S.L., et al., *Three Unique Interstitial Macrophages in the Murine Lung at Steady State.* Am J Respir Cell Mol Biol, 2017. **57**(1): p. 66-76.
35. Schyns, J., et al., *Non-classical tissue monocytes and two functionally distinct populations of interstitial macrophages populate the mouse lung.* Nat Commun, 2019. **10**(1): p. 3964.

36. Jin, H., et al., *Genetic fate-mapping reveals surface accumulation but not deep organ invasion of pleural and peritoneal cavity macrophages following injury.* Nat Commun, 2021. **12**(1): p. 2863.
37. Benard, A., et al., *Pleural Resident Macrophages and Pleural IRA B Cells Promote Efficient Immunity Against Pneumonia by Inducing Early Pleural Space Inflammation.* Front Immunol, 2022. **13**: p. 821480.
38. Dick, S.A., et al., *Three tissue resident macrophage subsets coexist across organs with conserved origins and life cycles.* Sci Immunol, 2022. **7**(67): p. eabf7777.
39. Ural, B.B., et al., *Identification of a nerve-associated, lung-resident interstitial macrophage subset with distinct localization and immunoregulatory properties.* Sci Immunol, 2020. **5**(45).
40. Cassado Ados, A., et al., *Cellular renewal and improvement of local cell effector activity in peritoneal cavity in response to infectious stimuli.* PLoS One, 2011. **6**(7): p. e22141.
41. Wang, C., et al., *Characterization of murine macrophages from bone marrow, spleen and peritoneum.* BMC Immunol, 2013. **14**: p. 6.
42. Isfort, K., et al., *Real-time imaging reveals that P2Y2 and P2Y12 receptor agonists are not chemoattractants and macrophage chemotaxis to complement C5a is phosphatidylinositol 3-kinase (PI3K)- and p38 mitogen-activated protein kinase (MAPK)-independent.* J Biol Chem, 2011. **286**(52): p. 44776-87.
43. Weber, G.F., et al., *Pleural innate response activator B cells protect against pneumonia via a GM-CSF-IgM axis.* J Exp Med, 2014. **211**(6): p. 1243-56.
44. Wang, X., et al., *IL-17A Promotes Pulmonary B-1a Cell Differentiation via Induction of Blimp-1 Expression during Influenza Virus Infection.* PLoS Pathog, 2016. **12**(1): p. e1005367.
45. Uderhardt, S., et al., *Resident Macrophages Cloak Tissue Microlesions to Prevent Neutrophil-Driven Inflammatory Damage.* Cell, 2019. **177**(3): p. 541-555 e17.
46. Kookoolis, A.S., et al., *Mortality of Hospitalized Patients with Pleural Effusions.* J Pulm Respir Med, 2014. **4**(3): p. 184.
47. Rosenstengel, A., *Pleural infection-current diagnosis and management.* J Thorac Dis, 2012. **4**(2): p. 186-93.
48. Califano, D., et al., *IFN-gamma increases susceptibility to influenza A infection through suppression of group II innate lymphoid cells.* Mucosal Immunol, 2018. **11**(1): p. 209-219.